Available online at www.sciencedirect.com
SCIENCE DIRECT®
Journal of Nuclear Materials 323 (2003) 251–262
journal of nuclear materials
www.elsevier.com/locate/jnucmat

Radiation and helium effects on microstructures, nano-indentation properties and deformation behavior in ferrous alloys

Y. Katoh [a,*], M. Ando [b], A. Kohyama [a]

[a] *Institute of Advanced Energy, Kyoto University, Gokasho, Uji, Kyoto 611-0011, Japan*
[b] *Japan Atomic Energy Research Institute, Naka, Ibaraki, Japan*

Abstract

Accelerated ion irradiation, especially 'dual-beam' irradiation, is a useful technique for experimental exploration of irradiation effects and validation of irradiation effect models, because of the unique controllability in irradiation conditions including the helium production rate. In this work, the effects of irradiation and helium implantation on microstructural evolution, hardness and plastic deformation behavior in Fe–15Cr–20Ni model austenitic ternary alloy and Fe–8 ~ 9Cr–2W reduced-activation martensitic steels were studied through combined applications of ion irradiation, nano-indentation, focused ion-beam microprocessing and transmission electron microscopy. Systematic data on irradiation hardening are presented for broad irradiation conditions. Influences of helium implantation on irradiation-induced microstructural and nano-indentation hardness changes were not detected in the Fe–8 ~ 9Cr–2W steels, while they were significant in the Fe–15Cr–20Ni alloy. The interaction behavior of dislocation loops with moving dislocations and the strength of the loops as obstacles to dislocation motion are also discussed for these two material classes based on the hardness, and the irradiated and indented microstructures.

PACS: 62.20.Fe; 62.20.Qp; 66.30.Jt; 66.30.Lw; 81.05.Bx

1. Introduction

Reduced-activation ferritic/martensitic (RAFM) steels are the prime candidate structural material for fusion reactor blanket / first walls, due mainly to their maturity as industrial materials and superior resistance to radiation-induced changes in their physical and mechanical properties [1]. Among the proposed RAFM steels, an Fe–8 ~ 9Cr–2W,V,Ta system has so far been recognized as the most promising material for the D-T fusion demonstration devices [2,3]. One of the most important remaining key technical issues for the RAFM steels as fusion structural material is the influence of transmutant helium production on the irradiation-related physical and mechanical property changes [1]. In particular, the potential existence of helium-embrittlement in irradiated RAFMs has been controversial for years [4].

The effects of helium production on irradiation damage in ferrous alloys have been studied using several simulation techniques. They include (a) fission neutron irradiation of isotopically tailored and/or nickel- or boron-doped materials [5], (b) very high energy proton or spallation neutron irradiation [6], (c) simultaneous irradiation of high energy metallic and helium ions [7] and (d) helium ion implantation in high voltage electron microscope. Among them, the simultaneous irradiation of self-ions and helium ions, or 'dual-beam' ion irradiation, is the only technique that produces fusion-relevant high energy cascades at any desired helium

* Corresponding author. Metals and Ceramics Division, Oak Ridge National Laboratory, P.O. Box 2008 Oak Ridge, TN 37831-6138, USA. Tel.: +1-865 576 5996; fax: +1-865 241 3650.
E-mail address: katohy@ornl.gov (Y. Katoh).

0022-3115/$ - see front matter © 2003 Elsevier B.V. All rights reserved.
doi:10.1016/j.jnucmat.2003.08.007

production (He/dpa) ratio for a 'single-parameter' experiment [8–10].

The major advantage of dual-beam ion irradiation is that any desired He/dpa ratio is achievable up to high doses under accurate control of temperature and other conditions. However, the application of dual-beam ion irradiation has mostly been limited to studies on microstructural modification. In ion irradiation experiments using static accelerators, the range of displacement damage is limited within a few microns from the irradiated surface. In dual-beam experiments, a range with (almost) constant He/dpa ratios is even smaller and typically less than 1 μm [7]. Therefore, it is very difficult to evaluate mechanical properties in a 'dual-beam irradiated' specimen, which actually is a very thin subsurface layer. For example, the depth profiles of atomic displacement damage and helium deposition in an Fe–9Cr–2W steel irradiated at DuET dual-beam facility are presented in Fig. 1 [8].

In order to enable mechanical property evaluation in ion-irradiated materials, application of the nano-indentation technique has been pursued [11–13]. Application of the dynamic indentation technique using load- and displacement-sensing instruments, which provides continuous 'apparent hardness' profiles of graded materials, enhanced the applicability of indentation technique to the ion-induced hardening evaluation [14]. Also, a technique for cross-sectional transmission electron microscopy (XTEM) of ion-irradiated and indented materials was developed [15]. This enabled examination of microstructures resulted from dislocation interactions with irradiation-produced defect features at different local plastic strain levels.

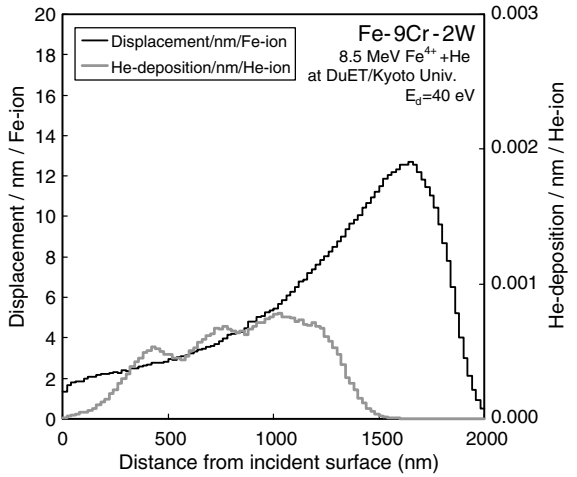

Fig. 1. The depth profiles of displacement damage and deposited helium ions in Fe–9Cr–2W steel for dual-beam irradiation at DuET Facility, Kyoto University. Calculation was made with TRIM-92 code assuming an average displacement threshold energy of 40 eV.

In this paper, experimental techniques developed in the course of exploring dual-beam ion irradiation effects on nano-indentation hardness (nano-hardness) and plastic deformation behavior in ferrous alloys will first be described. In the following part, the influence of simultaneous helium production on microstructural evolution and hardening in a model austenitic ternary alloy and Fe–8 ~ 9Cr–2W,V,Ta steels will be presented. Finally, the barrier strength and the contribution to plastic deformation behavior of irradiation-produced microstructural defects in these materials will be discussed.

2. Experimental

2.1. Materials

The materials used in this study were an Fe–15Cr–20Ni (mass percent) austenitic ternary model alloy, the Fe–9Cr–2W,V,Ta steel, JLF-1 [2] and Fe–8Cr–2W,V,Ta steel, IEA-heat F82H [3]. Actual chemical compositions of the materials are 15.0Cr–20.2Ni–0.006C–<0.005Si–0.0009P–0.0020S–0.0017N–0.0087O–0.003Co–balance Fe, 8.85Cr–1.99W–0.20V–0.080Ta–0.45Mn–0.10C–0.05Si–0.023N–balance Fe, and 7.71Cr–1.95W–0.16V-0.02Ta–0.16Mn–0.090C–0.11Si–0.0060N–balance Fe, respectively. The Fe–15Cr–20Ni alloy was solution-annealed at 1323 K for 30 min. prior to irradiation. The JLF-1 was normalized (1323 K × 60 min.) and tempered (1053 K × 60 min.) in its standard conditions. The IEA-heat F82H steel was prepared through normalization at 1313 K × 30 min. and tempered at 1023 K (standard condition) or 1073 K for 60 min. All the specimens were electrolytically polished to remove ~20 μm from the surface right before being subjected to irradiation.

2.2. Ion irradiation

The ion irradiation experiment was carried out at the High-fluence Irradiation Facility, University of Tokyo (HIT Facility) [7] and Multi-beam Materials Interaction Research Facility (DuET Facility), Kyoto University [8]. For the metallic ions, 4 MeV Ni ions were used at the HIT Facility, while ~8.5 MeV Fe ions were employed at the DuET Facility. The nominal fluence levels, which are approximately the average fluence levels over the dual-beam irradiated ranges, were up to 50 dpa. The nominal He/dpa ratio was also the average over the dual-beam irradiated range. The profiles of displacement damage level and deposited metallic and helium ions were calculated using TRIM-92 code, assuming a 40 eV of average displacement threshold energy [16]. The specimen temperature during irradiation was maintained within

±10 K of nominal temperature for the entire period of irradiation in each case.

2.3. Indentation and hardness profiling

Ultra-low load depth-sensing dynamic indentation was performed in a direction normal to the irradiated surface on all specimens. This method is effective only when a sufficiently even hardness profile is achieved for a certain thickness in the subsurface layer in the irradiated sample. Such conditions are reportedly confirmed in heavy ion-irradiated metals by cross-sectional nano-indentation work [11–13]. Akashi Co. (Zama, Japan) Model MZT-3 and Elionix Inc. (Tokyo, Japan) Model ENT-1100 instrumented nano-indentation devices were used. Triangular pyramidal diamond indenter tips with a 68° semiapex angle were employed in both instruments.

Nano-hardness profiles were obtained by a contact pressure evaluation method based on the procedure proposed by Oliver, et al. [17], where hardness, H, is defined as

$$H = \frac{P}{A(h_c)} \tag{1}$$

and P is the indentation load and A, as a function of contact depth (h_c), is the projected area of contact between the indenter and the specimen. In the current study, it was confirmed that sufficiently reproducible indentation hardness data could be obtained through this procedure for a fixed indentation depth of >100 nm. However, in this procedure, h_c was determined based on the load–displacement (P–h) property during the unloading process, and this prohibited the acquisition of a continuous hardness profile from a single indentation test. The displacement and helium deposition profiles shown in Fig. 1 may result in fairly complex hardness profile due to contributions by at least several layers with different features, e.g., the surface layer where the surface effect and the displacement effect dominate, the second layer where the displacement and the helium deposition are effective, the next layers where the displacement damage and/or deposited metallic ions influence, and the substrate which is free from the effect of irradiation. To evaluate the hardness of the 'dual-beam irradiated' layer, continuous hardness profile acquisition was performed in the following manner.

The P–h property during the unloading process is determined by a combination of (a) the effective elastic modulus of the material, (b) the contact depth h_c and (c) the projected area of contact $A = F(h_c)$. Therefore, if the irradiation-induced changes in elastic properties are negligible, the unloading P–h curve for a certain material using an identical indenter can be expressed as a function of h_c alone; $P = F_{\mathrm{UL}}(h_c, h)$. In this work, the expression of F_{UL} was simply made by a polynomial function fitted to unloading P–h curves obtained from an unirradiated specimen. It was confirmed that the unloading P–h curves obtained from irradiated specimens did not significantly deviate from F_{UL}. Therefore, the nano-hardness profile $H(h_c)$ is given as follows.

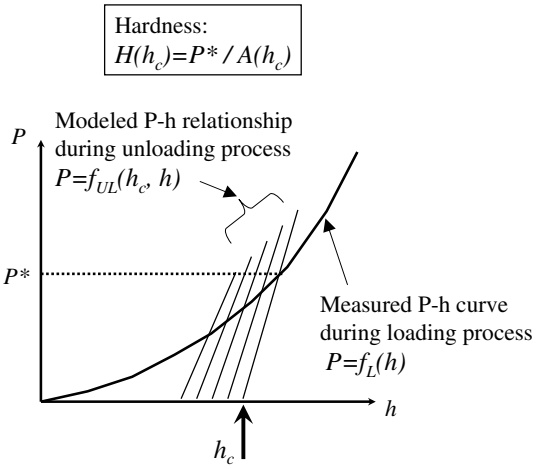

Fig. 2. Schematic illustration of the nano-indentation hardness profiling method by continuous stiffness estimation.

$$H(h_c) = \frac{P^*}{A(h_c)}. \tag{2}$$

In the above equation, P^* is the load at which the calibrated unloading function $P = F_{\mathrm{UL}}(h_c, h)$ intersects the loading curve $P = F_{\mathrm{L}}(h)$. This scheme, illustrated in Fig. 2, was effective to evaluate hardness changes in a variety of metallic materials induced by MeV range ion irradiation. Typical examples of $H(h_c)$ obtained by a single nano-indentation test on unirradiated and irradiated specimens are presented in Fig. 3. Fig. 3(a) confirms that the nano-hardness obtained by this method is sufficiently constant at $h_c > 100$nm. Hardness of the dual-beam irradiated range was determined from the plateau that appeared in an h_c range corresponding to (i.e., approximately 1/5 of) the dual-beam range [14]. An example of hardness profile with such a plateau obtained from a dual-beam irradiated sample is presented in Fig. 3(b).

2.4. Cross-sectional TEM

Cross-sectional thin foils from the irradiated and indented specimens were prepared using a JEOL (Tokyo, Japan) JFIB-2100 focused ion-beam (FIB) microprocessing device, so that each thin foil include the indentation axis and one of three sides of the indent. The ion beam used was gallium accelerated to 30 keV. During FIB-processing, the thin foils receive additional

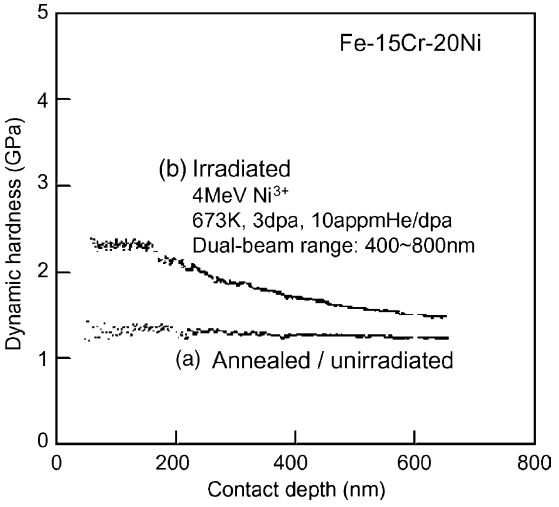

Fig. 3. Examples of continuous nano-hardness profiles, $H(h_c)$, obtained from unirradiated and irradiated Fe–15Cr–20Ni austenitic model ternary alloy.

irradiation damage and gallium ion deposition within their subsurface layers. These layers could completely be removed by electrolytic polishing for a few milliseconds. The microstructural examination was carried out using a JEOL JEM-2010EX transmission electron microscope (TEM) operating at 200 kV.

XTEM micrographs of the nano-indented Fe–15Cr–20Ni model alloy specimens are shown in Fig. 4(a) and (b) for an irradiation-free case. When the maximum contact depth during indentation is $<\sim$100 nm, as shown in Fig. 4(a), the dislocation microstructure is very anisotropic and characterized by preferred extension along $\langle 0\,1\,1\rangle$ family directions. Such anisotropic dislocation evolution could be a major factor in causing the relatively poor consistency in nano-hardness measurement on polycrystalline materials with a very small contact depth. On the contrary, the deformation volume becomes very semispherical when the contact depth exceeds about 300 nm, as shown in Fig. 4(b). The measured nano-hardness data at the contact depth of >200 nm are free from significant scatter. Therefore, we conclude that the isotropy of deformation volume could be one measure of data reliability in indentation tests.

3. Results and discussion

3.1. Irradiation-hardening and helium effect in Fe–15Cr–20Ni

The nano-hardness of unirradiated Fe–15Cr–20Ni austenitic model ternary alloy was consistent at 1.25 GPa. This nano-hardness corresponds to Vickers hardness number of 113, which agrees well with the typical hardness number of austenitic model alloys in a solution-annealed condition. Ion irradiation caused significant hardening regardless of helium co-implantation at temperatures of 473–773 K. In Fig. 5, the hardness changes in the model alloy during 4 MeV nickel ion irradiation at 473–873 K are plotted against ion fluence level. The irradiated microstructures at 473, 573 and 673 K mostly consisted of Frank dislocation loops, a smaller amount of perfect loops, and irresolvable 'black-spot' defects up to 10 dpa (Fig. 6). The loop microstructures were very similar at 473 and 573 K, but the development rate was slower at 473 K. The dislocation microstructure became significantly coarser when the irradiation temperature was increased to 673 K. At 773 K, perfect loops and network dislocations dominated by 3 dpa. The time evolution of irradiated hardness in Fig. 5 is clearly reflecting the microstructural development.

In Fig. 7, the influence of helium co-implantation on the temperature dependence of irradiation-hardening at 10 dpa is presented. The presence of helium moderated irradiation hardening at $T < 673$ K while it did not impose an obvious effect at $T > 773$ K. At $T < 673$ K, the dislocation loop development was clearly retarded by the presence of helium, which presumably resulted in reduced irradiation hardening. At $T > 773$ K, the dual-beam irradiated materials developed significant amount of cavities. These cavities must have contributed to the hardening. The cavity microstructures at 10 dpa are presented in Fig. 8 for the cases of 773 and 873 K dual-beam irradiation.

3.2. Hardening mechanism in Fe–15Cr–20Ni

It is very difficult to correlate indentation hardness with more commonly accepted mechanical properties such as uniaxial tensile properties. This is mainly because of the complex stress state and the widely varied plastic strain levels in indented specimens. However, it is reported that the hardening obtained by indentation tests approximately correlates with the increase in tensile yield stress in the following relationship [18].

$$\Delta H \cong 3\Delta\sigma_y. \tag{3}$$

Using this relationship, it is possible to compare the amount of irradiation hardening with predicted hardening based on the microstructural data and Orowan's dispersion strengthening model for planar defects [19]:

$$\Delta\sigma_y = MGb(Nd)^{1/2}/\beta, \tag{4}$$

where $M = \sim 3.1$ for cubic polycrystals [20], G = shear modulus, b = Burger's vector magnitude, N = defect number density, d = defect diameter and $1/\beta$ = barrier strength coefficient which usually falls between 2.2 and 3.0 [19].

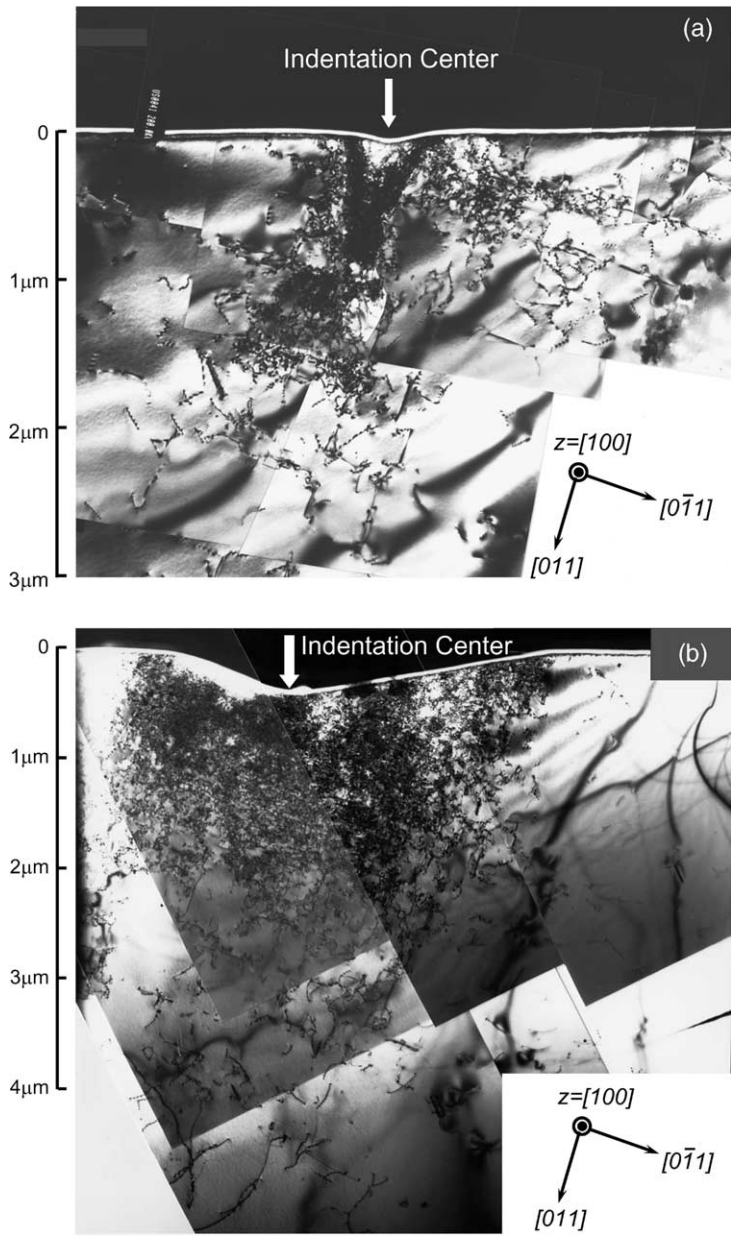

Fig. 4. Cross-sectional transmission electron microscopy (XTEM) of Fe–15Cr–20Ni austenitic model ternary alloy after indentation to the maximum contact-depths of ~100 nm (a) and ~380 nm (b).

In Fig. 9, the experimentally obtained ΔH divided by the model-predicted ΔH using Eqs. (3) and (4) and taking $\beta = 3$ [21] is plotted as a function of mean dislocation loop diameter. The apparent feature of Fig. 9 is that the effective barrier strength coefficient for dislocation loops become larger when the loop diameter is smaller then approximately 15 nm. This suggests that the effective interaction cross-sections for small loops are much larger than their physical sizes due to the relatively large strain field. At the same time, all the specimens which exhibited substantially larger hardening than the model prediction had been irradiated at <573 K. Therefore, there might be radiation-induced microstructural or microchemical changes that do not occur at higher temperatures but strongly contribute to hardening. It is also possible that a part of defects responsible for the low-temperature hardening were not visible. The 'black-spot' defects are not likely being the cause,

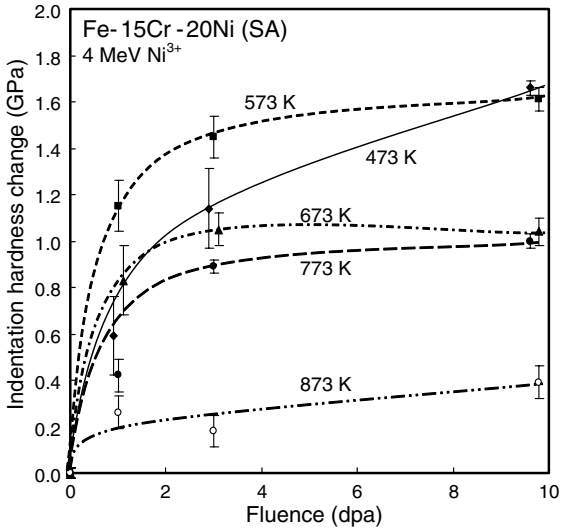

Fig. 5. Fluence-dependence of nano-indentation hardness in Fe–20Ni–15Cr during single-beam ion irradiation. The error bars shows standard deviation. Horizontal positions of data points are intentionally shifted for readability, while nominal fluences were 1.0, 3.0 and 10.0 dpa in this experiment.

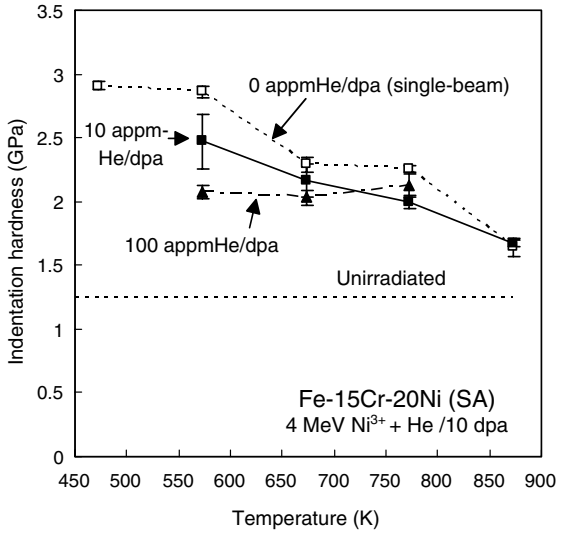

Fig. 7. The influence of He/dpa ratio on temperature dependence of irradiated hardness in Fe–15Cr–20Ni alloy at 10 dpa.

because their appearance is not significantly different between 573 and 673 K irradiation cases as far as examined with a conventional TEM.

The result of XTEM analysis on the irradiated and indented Fe–15Cr–20Ni alloy has been published elsewhere [22]. There, we reported that the majority of irradiation-produced dislocation loops had disappeared after indentation. When the indentation-induced plastic deformation range was about 1200 nm, dislocation loops completely annihilated within about 800 nm from the contact center. Between 800 and 1200 nm from the contact center, more than 80% of the dislocation loops disappeared. Interestingly, as shown in Fig. 10, Frank loops with smaller diameter tended to disappear more effectively, in spite of the smaller apparent reaction cross-sections with gliding dislocations. This observation supports the relatively low activation energies for small Frank loop motion in clean fcc metals and alloys and the motions could be driven by the strain field [23,24]. A combination of the possibly strong barrier strength and the easy motion (only when certain conditions are met) could cause plastic instability in low temperature-irradiated austenitics. On the other hand, the appearance of black-spot defects was not strongly affected even in the regions which had undergone heavy deformation. Therefore, defects of this type could be a stable hardening source in austenitic alloys. The black-spot type defects are believed mostly to be vacancy

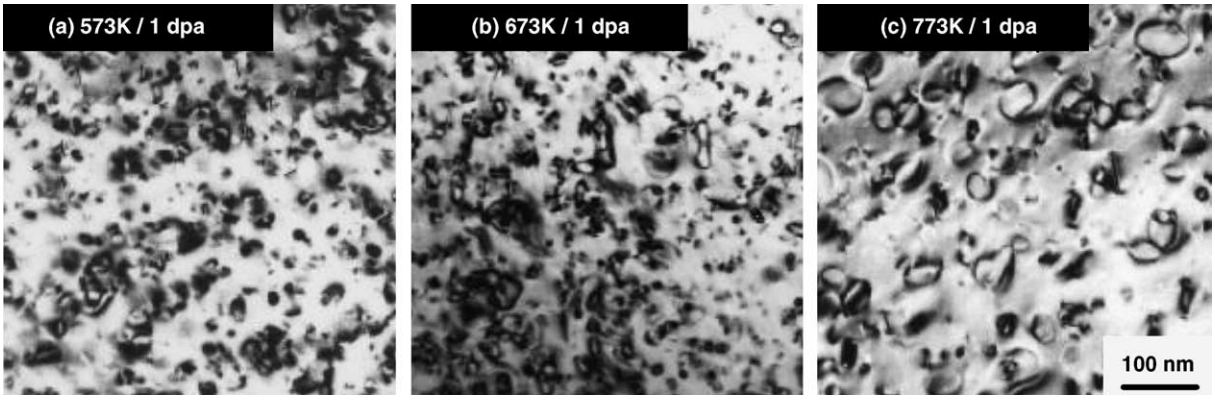

Fig. 6. Microstructures in Fe–15Cr–20Ni alloy after single-beam ion irradiation at 573, 673 and 773 K.

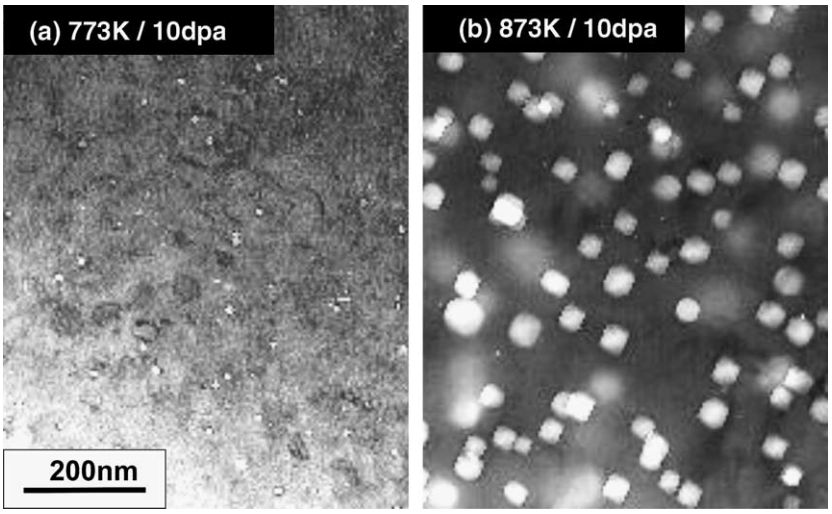

Fig. 8. Cavity microstructures in Fe–15Cr–20Ni alloy after dual-beam (10 appmHe/dpa) ion irradiation to 10 dpa at 773 and 873 K.

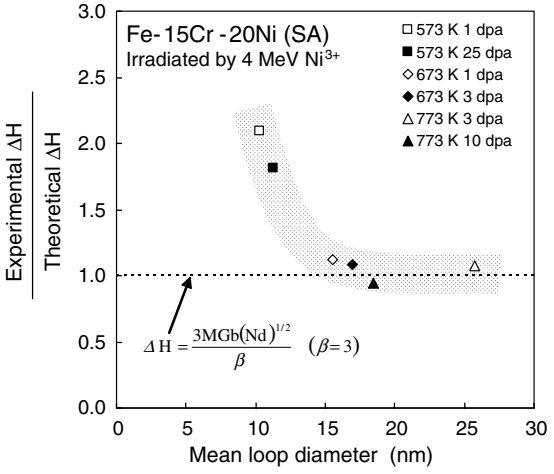

Fig. 9. Experimentally obtained hardening amount (ΔH) in Fe–15Cr–20Ni alloy divided by model-estimated ΔH (see text) plotted as a function of mean dislocation loop diameter.

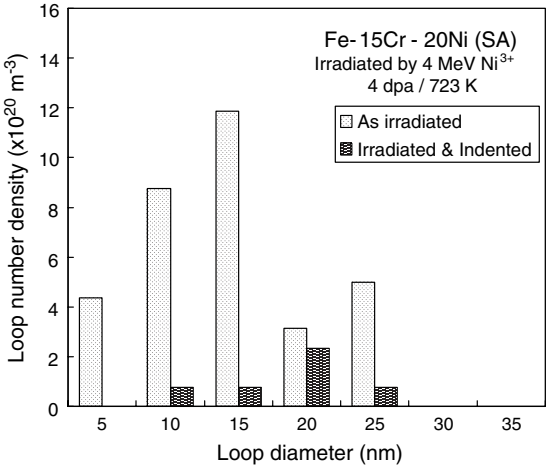

Fig. 10. Frank loop size distribution in ion-irradiated Fe–15Cr–20Ni alloy before and after nano-indentation.

clusters, because many of them collapse into stacking fault tetraherda after annealing at ~773 K.

The hardening by cavities was also examined in a similar way. In Fig. 11, the experimentally determined cavity hardening in the Fe–15Cr–20Ni alloy is compared with a model estimation by Scattergood and Bacon [25]:

$$\Delta\sigma_y = M \cdot \frac{\alpha G b (Nd)^{1/2}}{1 - 0.81 d (Nd)^{1/2}} \times \ln\left\{ \frac{0.81 d}{3.3 b} [1 - 0.81 d (Nd)^{1/2}] \right\}, \quad (5)$$

where α = barrier strength factor and taken as 1 in this analysis. This result shows that the effective barrier strength factor for cavities are 0.1–0.3 instead of 1 that has usually been taken [26]. Other cavity-hardening models, including revised Orowan's model and Weeks' model, give similar results to Fig. 11 [27,28]. This is probably because cavities produced in the model alloy during ion irradiation up to 25 dpa are relatively clean, while solute segregation and associated precipitation are playing a major role in neutron hardening in austenitic steels for which $\alpha = 1$ is generally applicable [26]. It should also be noted that omitting the Taylor factor in Eq. (5) in some work on neutron hardening analysis has contributed to this discrepancy.

XTEM of indented cavity microstructure composed of severely stretched cavities and network dislocations.

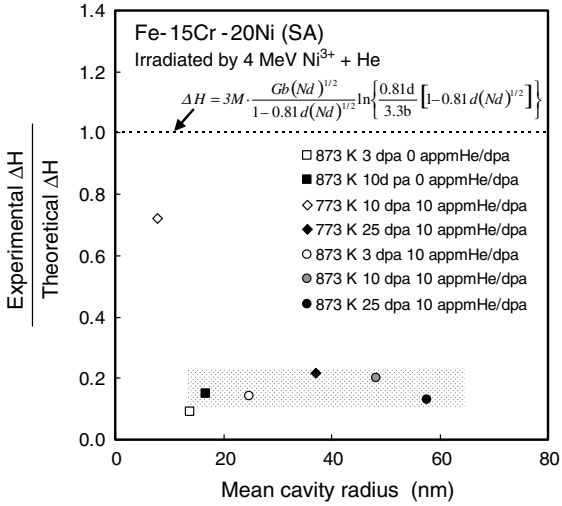

Fig. 11. Experimentally obtained cavity-hardening (ΔH) in Fe–15Cr–20Ni alloy divided by model-estimated ΔH (see text) plotted as a function of mean cavity radius.

Many dislocation segments were terminated on the cavity surfaces and the end segments were always roughly normal to them. Therefore, the model by Scattering and Bacon seems most applicable to this case. This implies that dislocation attraction on cavity surfaces through an image force is the dominating hardening mechanism and cavity cutting by dislocations is the operating deformation mechanism.

3.3. Irradiation-hardening and helium effect in Fe–8∼9Cr–2W RAFMs

The average nano-hardness for JLF-1 and F82H specimens after normalizing and tempering in respective standard conditions was 2.2–2.4 GPa. This nano-hardness corresponds to a Vickers hardness number of 203–221, which agrees well with the Vickers hardness, 213–222, measured with the load of 98N [3,29]. The scatter range of hardness data from a single specimen was typically ±0.2 GPa, which was significantly larger than that for the austenitic alloys. This is probably due to the influence of inhomogeneous dislocation microstructure, crystallographic orientation and anisotropic martensitic lath structures. In this work, therefore, at least five indentation measurements were made in different prior austenitic grains within a single specimen and the average was taken as the specimen's nano-hardness for a given h_c range.

In Fig. 12, the time-evolution of hardness of JLF-1 during single- and dual-beam irradiation at 573–773 K is presented. The amount of irradiation hardening was not very significant (10–40%) up to 10 dpa, in contrast to ∼130% in the austenitic model alloy. The scatter in dual-beam irradiated hardness was relatively large (∼13% in standard deviation), partly because of the smaller range of helium deposition. However, the data obtained sug-

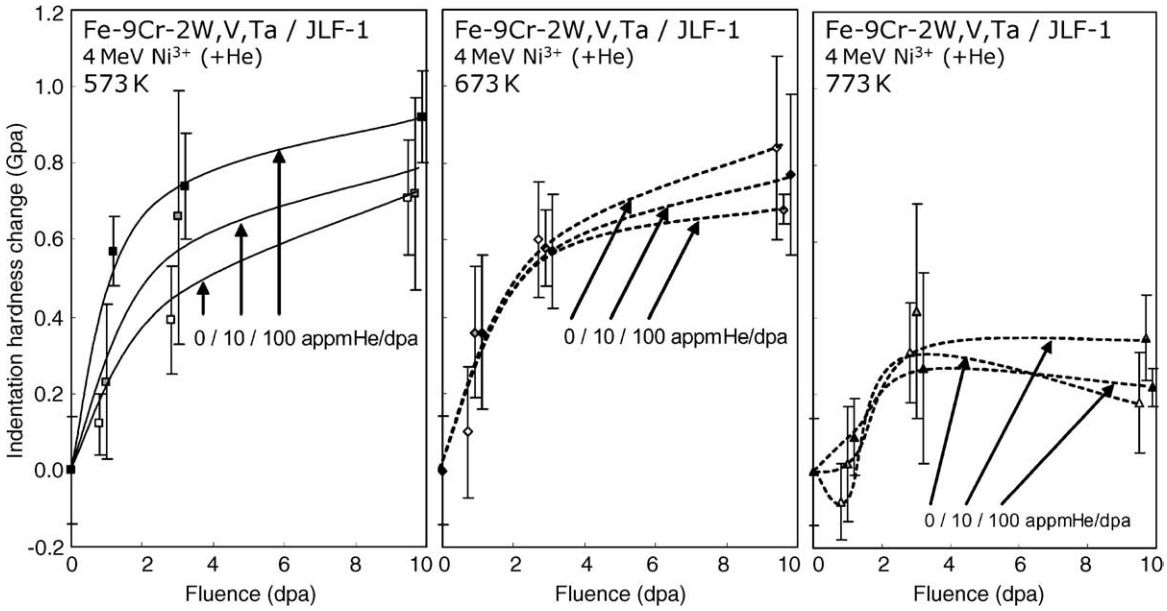

Fig. 12. Fluence-dependence of nano-indentation hardness changes in Fe–9Cr–2W reduced-activation martensitic steel (JLF-1) during single- and dual-beam ion irradiation. The error bars show standard deviation. Horizontal positions of data points are intentionally shifted for readability, while nominal fluences were 1.0, 3.0 and 10.0 dpa in this experiment.

gests that an obvious helium effect on irradiation hardening could have occurred only at 573 K. At $T > 773$K, irradiation-softening was clearly observed at 1 dpa in single-beam irradiation. Corresponding recovery of dislocation structures within martensitic laths in the near-surface layer, typically to a depth of ~500 nm for the case of 773 K irradiation, was observed by TEM. Such a thermal recovery and the resultant softening did not occur during dual-beam irradiation. In other word, the presence of only small amount (~10 ppm) of helium was effective in retarding a thermal recovery of the characteristic microstructure for martensitic steels.

An attempt to compile the hardening at 5–10 dpa as a function of irradiation temperature is made in Fig. 13. A hardening peak is likely to occur at around 623 K. The hardening rapidly becomes less significant at higher temperatures, and the difference between JLF-1 and F82H might be appearing only in this temperature range. Such difference could have occurred not only by minor difference in the alloy composition and heat treatment but also by the differences in irradiating particles (JLF-1 was irradiated by nickel ions). The estimated concentration of deposited nickel at the midplane of dual-beam range is 60 ppm/dpa. Actual nickel concentration could be higher because of the potential migration from the deeper regions where nickel concentration is higher. A very significant enhancement of irradiation hardening at 623 K by nickel addition is reported for F82H [30].

The single- and dual-beam irradiated microstructures in the standard F82H at the peak hardening temperature are shown in Fig. 14. The observed microstructural defects that had been produced by irradiation were small dislocation loops and 'black-spot' defects. Majority of the observed loops were of $(a/2)\langle 1\,1\,1\rangle$ type. Quantitative features of these defects were not significantly affected by helium co-implantation, as seen in Fig. 15(a) and (b), where the average size and the number density, respectively, are plotted against fluence level.

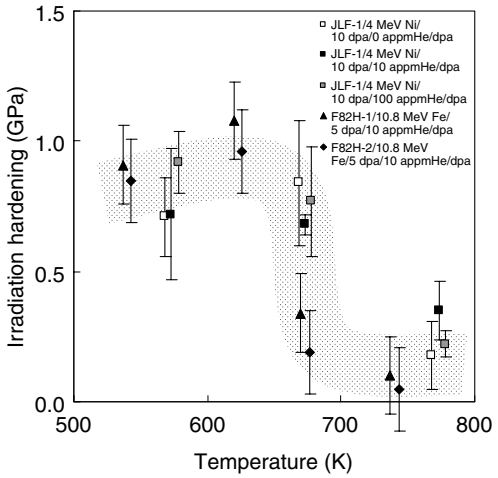

Fig. 13. Irradiation temperature dependence of hardening amount (ΔH) in Fe–8 ~ 9Cr–2W reduced-activation martensitic steels by single- and dual-beam ion irradiation to 5–10 dpa. F82H-1 and -2 are IEA-heat F82H which had been tempered at 1023 and 1073 K, respectively.

3.4. Hardening mechanism in Fe–8 ~ 9Cr–2W RAFMs

With the quantitative microstructural data in Fig. 15 and taking $\beta = 2.5$, Eqs. (3) and (4) give a reasonable

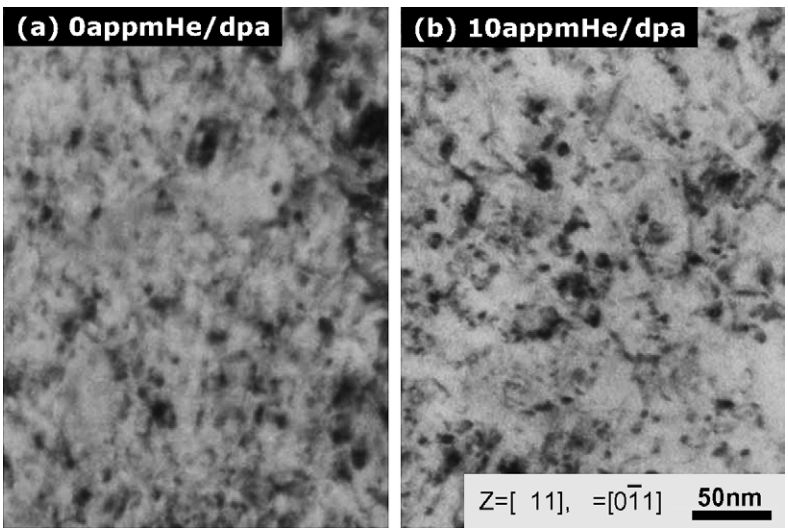

Fig. 14. Irradiation-produced microstructural damages in Fe–8Cr–2W steel (IEA-heat F82H) after single- (Fe ions) and dual-beam (Fe + He ions, 10 appmHe/dpa) irradiation to 50 dpa at 623 K.

estimation of indentation hardening in Fe–8 ~ 9Cr–2W RAFMs irradiated at $T < 623$ K, in comparison with the corresponding experimental data [30]. Therefore, it is likely that the small dislocation loops and black-spot defects are the primary hardening sources and Orowan's dispersion strengthening is the working mechanism for these cases.

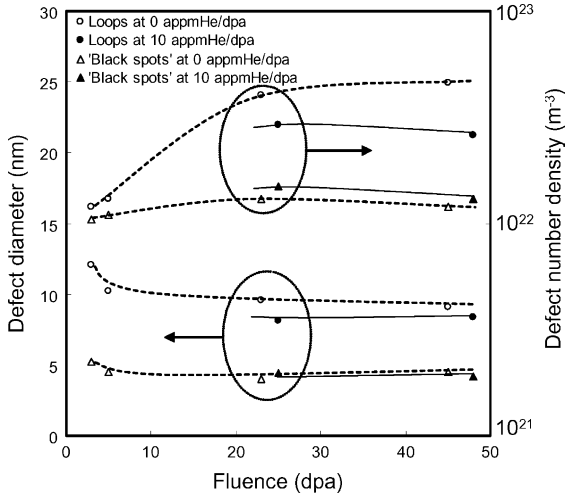

Fig. 15. The evolutions of size and number density of irradiation-produced dislocation loops and 'black-spot' defects in Fe–8Cr–2W steel (IEA-heat F82H) during single- (Fe ions) and dual-beam (Fe + He ions, 10 appmHe/dpa) irradiation at 623 K.

XTEM of the irradiated and indented specimen was also performed for the standard IEA-heat F82H steel irradiated with iron ions (single beam) at 623 K for 5 dpa, in the same way as the austenitic model alloy. A low magnification micrograph of an entire cross-section of the indentation-induced plastic deformation zone is presented in Fig. 16(a). The deformation zone was roughly semispherical but more irregular-shaped and inhomogeneous in dislocation density than in the indented austenitic model alloy. Another noticeable feature in Fig. 16 is that the number density of dislocation loops is substantially reduced within the plastic deformation volume. This trend is obvious when the unindented and indented microstructures are compared between Fig. 16(b) and (c).

In Fig. 17, number density of dislocation loops at different distances from the irradiated surface is compared for before and after indentation. For the 'after indentation' case, the distance from the irradiated surface is equal to that from the indentation center. About 50% of the irradiation-produced dislocation loops annihilated through the indentation. If the loop size distributions are closely examined, it is noticed that the loops larger than ~10 nm in diameter have almost

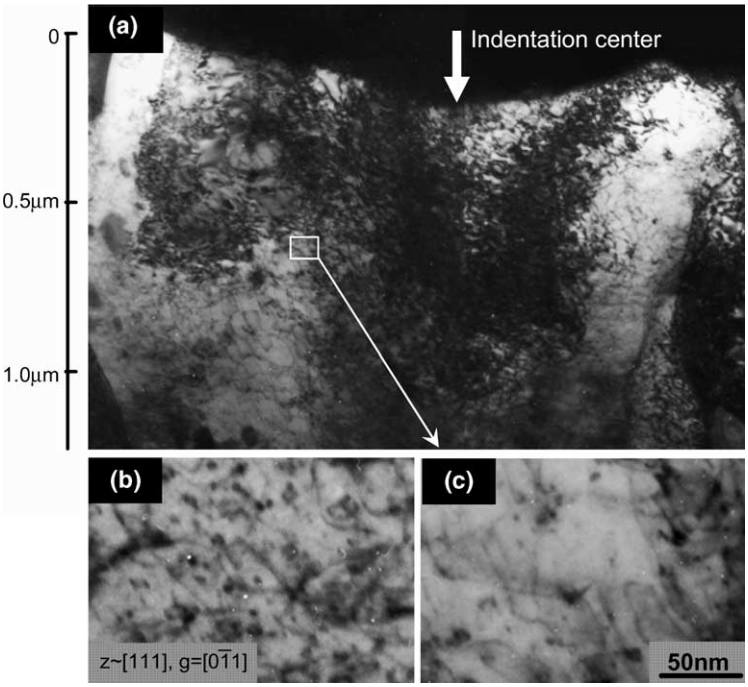

Fig. 16. An entire cross-section of the indentation-induced plastic deformation zone (a) and higher magnification images of irradiated (b) and then indented (c) microstructures in Fe–8Cr–2W steel (IEA-heat F82H). The specimen was irradiated with 6.4 MeV Fe ions to 5 dpa at 623 K.

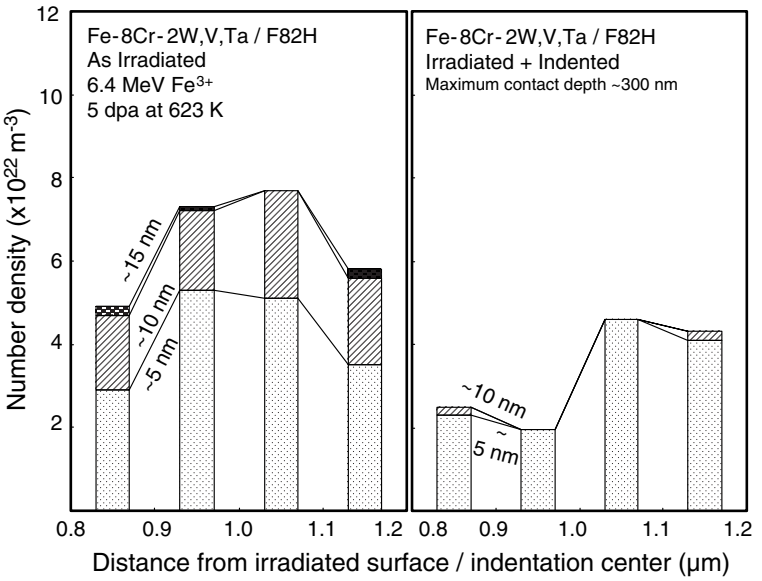

Fig. 17. Comparison of dislocation loop number density before and after nano-indentation in irradiated Fe–8Cr–2W steel (IEA-heat F82H). The sizes indicated within charts represent loop diameters measured on weak beam dark field images.

completely disappeared. On the other hand, 80% of the loops smaller than ~5 nm have survived. Therefore, it is very clear that larger dislocation loops have larger reaction cross-section with the gliding dislocations and that small dislocation loops could be stable hardening sources in these materials.

4. Conclusions

The effects of irradiation and helium production on microstructural evolution, hardness and plastic deformation behavior in Fe–15Cr–20Ni model austenitic alloy and Fe–8~9Cr–2W RAFMs were studied by combined application of ion (including 'dual-beam') irradiation, nano-indentation, FIB microprocessing and (X)TEM. For this purpose, a method for continuous nano-hardness profiling of ion irradiated materials was successfully developed. Also, a method for XTEM of nano-indented alloy samples was established.

Systematic data on irradiation hardening are presented for broad irradiation conditions. The austenitic alloy exhibited severe (~130%) hardening by single-beam irradiation. Helium co-implantation mildly moderated the irradiation hardening in the studied condition range. In the RAFMs, the extent of irradiation hardening was moderate (~40%) and insensitive to the presence of helium. Microstructural examination generally supported these observations.

Commonly used hardening models failed to explain irradiation hardening when small Frank loops or cavities are the dominating radiation defect features in the austenitic alloy. This is probably because small Frank loops have larger effective interaction cross-sections with gliding dislocation than their actual sizes, and the relatively clean cavities produced by ion irradiation are much weaker deformation barriers than the neutron-produced decorated cavities.

The result of indented XTEM suggested that small dislocation loops in the austenitic alloy could be an unstable deformation barrier, while other defects (cavities and 'black-spot' defects in the austenitic alloy and dislocation loops and 'black-spot' defects in the RAFMs) are stable during plastic deformation.

Acknowledgements

The authors would like to thank Dr H.Tanigawa at Japan Atomic Energy Research Institute for useful discussion.

References

[1] R.L. Klueh, D.S. Gelles, S. Jitsukawa, A. Kimura, G.R. Odette, B. van der Schaaf, M. Victoria, J. Nucl. Mater. 307–311 (2002) 455.
[2] T. Hasegawa, Y. Tomita, A. Kohyama, J. Nucl. Mater. 258–263 (1998) 1153.
[3] K. Shiba, A. Hishinuma, A. Tohyama, K. Kasamura, Properties of Low Activation Ferritic Steel F82H IEA Heat, JAERI-Tech 97-038, JAERI, 1997.
[4] A. Kimura, R. Kasada, K. Morishita, R. Sugano, A. Hasegawa, K. Abe, T. Yamamoto, H. Matsui, N. Yoshida,

B.D. Wirth, T.D. Rubia, J. Nucl. Mater. 307–311 (2002) 521.
[5] D.S. Gelles, M.L. Hamilton, B.M. Oliver, L.R. Greenwood, S. Ohnuki, K. Shiba, Y. Kohno, A. Kohyama, J.P. Robertson, J. Nucl. Mater. 307–311 (2002) 212.
[6] L.L. Snead, R.E. Stoller, M.A. Sokolov, S. Maloy, J. Nucl. Mater. 307–311 (2002) 187.
[7] Y. Kohno, K. Asano, A. Kohyama, K. Hasegawa, N. Igata, J. Nucl. Mater. 141–143 (1986) 794.
[8] A. Taylor, D.G. Ryding, J. Wallace, B. Okray Hall, D.I. Potter, in: Proceedings of the International Conference on Radiation Effects and Tritium Technology for Fusion Reactors, Gatlinburg, 1975, p. 1.
[9] M.B. Lewis, N.H. Packan, G.F. Wells, R.A. Guhl, Nucl. Instrum. and Meth. 167 (1979) 233.
[10] A. Kohyama, Y. Katoh, M. Ando, K. Jimbo, Fusion Eng. Des. 51&52 (2000) 789.
[11] S.J. Zinkle, W.C. Oliver, J. Nucl. Mater. 141–143 (1986) 548.
[12] D.H. Plantz, L.M. Wang, R.A. Dodd, G.L. Kulcinski, Matell. Trans. 20A (1989) 2681.
[13] P.M. Rice, R.E. Stoller, G.E. Lucas, W.C. Oliver, Proc. Mater. Res. Soc. Symp. 373 (1995) 149.
[14] Y. Katoh, H. Tanigawa, T. Muroga, T. Iwai, A. Kohyama, J. Nucl. Mater. 271&272 (1999) 115.
[15] M. Ando, Y. Katoh, H. Tanigawa, A. Kohyama, J. Nucl. Mater. 271&272 (1999) 111.
[16] J.P. Biersack, L.G. Haggmark, Nucl. Instrum. and Meth. 174 (1980) 257.
[17] W.C. Oliver, G.M. Pharr, J. Mater. Res. 7 (1992) 1564.
[18] G.E. Lucas, G.R. Odette, R. Maiti, J.W. Sheckherd, Influence of Radiation on Material Properties, ASTM STP 956, ASTM, Philadelphia, 1987, p. 379.
[19] J.W. Martin, Micromechanisms in Particle-Hardened Alloys, Cambridge University, Cambridge, 1980.
[20] U.F. Kocks, Metall. Trans. 1 (1970) 1121.
[21] R.E. Stoller, Effects of Radiation on Materials, ASTM STP 1270, ASTM, Philadelphia, 1996, p. 25.
[22] M. Ando, Y. Katoh, H. Tanigawa, A. Kohyama, T. Iwai, J. Nucl. Mater. 283–287 (2000) 423.
[23] Yu.N. Osetsky, D.J. Bacon, Nucl. Instrum. and Meth. B 202 (2003) 31.
[24] K. Morishita, T. Diaz de la Rubia, A. Kimura, Nucl. Instrum. and Meth. B 180 (2001) 66.
[25] R.O. Scattergood, D.J. Bacon, Acta Metall. 30 (1982) 1665.
[26] G.E. Lucas, J. Nucl. Mater 206 (1993) 287.
[27] D.J. Bacon, U.F. Kocks, R.O. Scattergood, Philos. Mag. 28 (1973) 1241.
[28] R.W. Weeks, S.R. Pati, M.F. Ashby, P. Barrand, Acta Metall. 17 (1969) 1403.
[29] N. Inoue, T. Muroga, A. Nishimura, T. Nagasaka, O. Motojima, S. Uchida, H. Yabe, K. Oguri, Y. Nishi, Y. Katoh, A. Kohyama, J. Nucl. Mater. 283–287 (2000) 1187.
[30] M. Ando, H. Tanigawa, S. Jitsukawa, T. Sawai, Y. Katoh, A. Kohyama, K. Nakamura, H. Takeuchi, J. Nucl. Mater. 307–311 (2002) 260.